Published in partnership with Nanjing University



https://doi.org/10.1038/s41535-025-00739-6

# Magnetic memory and distinct spin populations in ferromagnetic Co<sub>3</sub>Sn<sub>2</sub>S<sub>2</sub>

Check for updates

Charles Menil ®¹ ⊠, Brigitte Leridon ®¹, Antonella Cavanna², Ulf Gennser², Dominique Mailly², Linchao Ding³, Xiaokang Li³, Zengwei Zhu ®³, Benoît Fauqué ®⁴ & Kamran Behnia ®¹

Co<sub>3</sub>Sn<sub>2</sub>S<sub>2</sub>, a ferromagnetic Weyl semi-metal with Co atoms on a kagome lattice, has generated much recent attention. Experiments have identified a temperature scale below the Curie temperature. Here, we find that this magnet keeps a memory, when not exposed to a magnetic field sufficiently large to erase it. We identify the driver of this memory effect as a small secondary population of spins, whose coercive field is significantly larger than that of the majority spins. The shape of the magnetization hysteresis curve has a threshold magnetic field set by the demagnetizing factor. These two field scales set the hitherto unidentified temperature scale, which is not a thermodynamic phase transition, but a crossing point between meta-stable boundaries. Global magnetization is well-defined, even when it is non-uniform, but drastic variations in local magnetization point to a coarse energy landscape, with the thermodynamic limit not achieved at micrometer length scales.

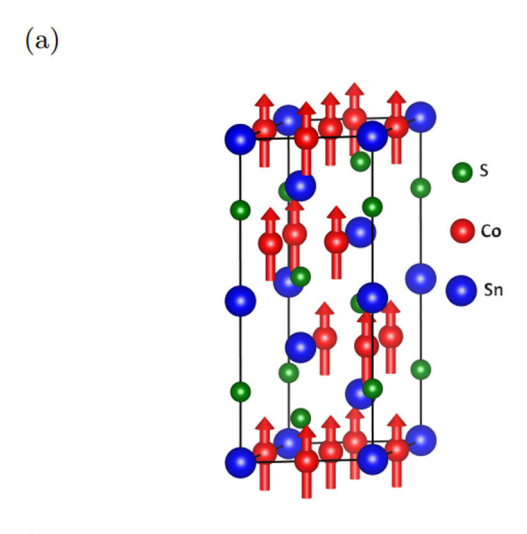
First synthesized as a ternary chalcogenide with Shandite structure, Co<sub>3</sub>Sn<sub>2</sub>S<sub>2</sub> became a subject of tremendous attention after its identification as a ferromagnetic Weyl semi-metal<sup>2,3</sup>. It crystallizes in a rhombohedral structure with R3m space group (n°166). The cobalt atoms form kagome sheets in the ab plane, which are separated by blocks of Sn and S atoms (see Fig. 1a). It magnetically orders below  $T_C \approx 175 \,\mathrm{K}$  with a saturation moment of  $\approx 0.3 \,\mu_B$  per Co atom<sup>4</sup>, and with the easy axis residing along the c-axis. Ab initio band calculations<sup>5</sup>, as well as photoemission<sup>6</sup> and Mössbauer experiments<sup>7</sup> identified it as a ferromagnetic half-metal. It is also a semi-metal with an equally low concentration of electrons and holes ( $n = p \simeq 8.7 \times 10^{-19} \text{cm}^{-3}$ ). Thanks to such a low carrier density (comparable to elemental antimony, where  $n = p \simeq 6.6 \times 10^{-19} \, \text{cm}^{-3}$ ), mobility is sufficiently large to detect quantum oscillations and experimentally confirm the theoretically computed Fermi surface, consisting of two electron-like and two hole-like and multiply degenerate sheets9.

The low carrier density implies that each mobile electron is shared by several hundred formula units of  $\text{Co}_3\text{Sn}_2\text{S}_2$ . This distinct feature leads to an exceptionally large anomalous Hall angle<sup>2</sup>. Indeed, although the anomalous Hall conductivity of  $\text{Co}_3\text{Sn}_2\text{S}_2$  ( $\sigma_{xy}^A(2\text{K}) \simeq 1200(\Omega\text{cm})^{-1}$  <sup>2,8</sup>) falls below what is seen in  $\text{CoMn}_2\text{Ga}$  ( $\sigma_{xy}^A(2\text{K}) \simeq 2000(\Omega\text{cm})^{-1}$  <sup>10</sup>), the anomalous Hall angle attains a record magnitude ( $\frac{\sigma_{xy}^A}{\sigma_{xx}}(120\text{ K}) \simeq 0.2$ ) in  $\text{Co}_3\text{Sn}_2\text{S}_2^2$ . Another consequence of high mobility is seen in the Nernst response. In contrast with low-mobility topological magnets (like Mn<sub>3</sub>X (X=Sn, Ge) in which the

Nernst effect is purely anomalous  $^{11-13}$ ),  $Co_3Sn_2S_2$  has a sizeable ordinary Nernst response in addition to the anomalous component. Their ratio can be tuned by changing the concentration of impurities.

Together with Fe<sub>3</sub>Sn<sub>2</sub><sup>14</sup>, Co<sub>3</sub>Sn<sub>2</sub>S<sub>2</sub> belongs to the restricted family of kagome ferromagnets. However, several recent experimental studies 15-26 suggested that the magnetic ordering in Co<sub>3</sub>Sn<sub>2</sub>S<sub>2</sub> is not purely ferromagnetic. In addition to the Curie temperature ( $T_C \simeq 175 \,\mathrm{K}$ ), there is an additional temperature scale,  $T_A$ . Muon spin-rotation ( $\mu_{SR}$ ) measurements<sup>15</sup> suggested the presence of an in-plane anti-ferromagnetic component emerging above 90 K that occupies an increasing volume fraction with warming and becomes dominant above 150 K. A Kerr microscopy study<sup>17</sup> reported that near  $T_A \simeq 135$  K, domain wall mobility goes through a deep minimum, pointing to a phase transition within the domain walls. A recent neutron scattering study<sup>18</sup> found no evidence for antiferromagnetism in the magnetically ordered state and attributed the features observed near 125 K to a reduction of ferromagnetic domain size. Another study<sup>19</sup> found that an anti-ferromagnetic component emerges with indium doping in Co<sub>3</sub>Sn<sub>2</sub>S<sub>2</sub>. Lachman et al.<sup>21</sup> found that the hysteresis loop of the anomalous Hall effect is not centered around zero field, a feature reminiscent of the so-called "exchange bias" effect in ferromagnet/antiferromagnet bilayers<sup>27</sup>. Moreover, they found that the magnetization hysteresis loop, which has a rectangular shape at low temperature, displays a "bow-tie" structure above  $T_A \simeq$ 125 K. This led them to suggest the existence of a spin-glass phase.

<sup>1</sup>Laboratoire de Physique et d'Étude des Matériaux, (ESPCI - CNRS - Sorbonne Université), Université Paris Sciences et Lettres, 75005 Paris, France. <sup>2</sup>Centre de Nanosciences et de Nanotechnologies, CNRS, Université Paris-Saclay, 91120 Palaiseau, France. <sup>3</sup>Wuhan National High Magnetic Field Center and School of Physics, Huazhong University of Science and Technology, Wuhan, 430074, China. <sup>4</sup>JEIP (USR 3573 CNRS), Collège de France, Université Paris Sciences et Lettres, 75005 Paris, France. — e-mail: charles.menil@espci.fr



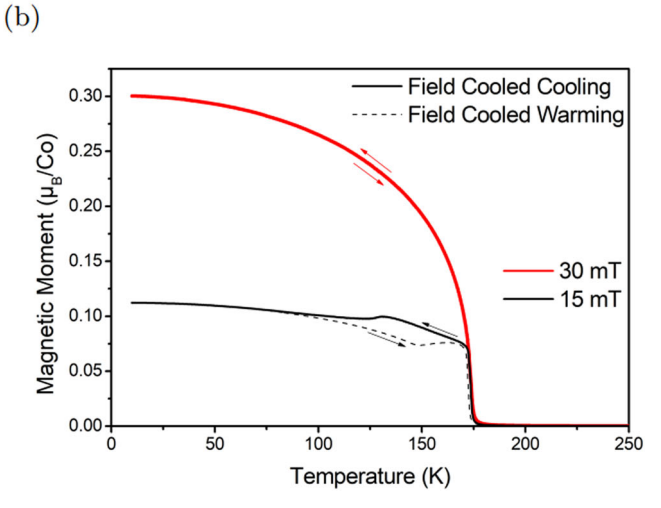


Fig. 1 | Crystal structure of  $Co_3Sn_2S_2$  and magnetization versus temperature. a Crystal structure of  $Co_3Sn_2S_2$  with arrows showing the orientation of spins in the ordered phase. b Magnetization as a function of temperature at several magnetic fields. Above 22 mT, magnetization in the ferromagnetic phase is featureless. But when the sample is cooled down in presence of a magnetic field smaller than this threshold field, there is an anomaly and a hysteresis, which extends down to  $\simeq 110$  K.

Zivkovic et al.<sup>22</sup> reported a similar change in the shape of the magnetic hysteresis loop and diagnosed a phase transition at  $T_A \simeq 128\,\mathrm{K}$  associated with a change in the canting angle of the magnetic moment away from the c-axis. On the other hand, Avakyants et al.<sup>23</sup>, employing a First Order Reversal Curves (FORC) analysis, concluded that two independent magnetic phases coexist below  $T_C$ . Noah et al.<sup>24</sup> reported that the exchange bias found in this system<sup>21</sup> can be tuned by changing the prior history of the sample.

Here, we present a systematic study of magnetization as a function of temperature, magnetic field and prior magnetic history in  $\text{Co}_3\text{Sn}_2\text{S}_2$  single crystals and identify the origin of  $T_A$ . We find that the "bow-tie" shape of the hysteresis  $\text{loop}^{21,25,28}$  is not restricted to temperatures exceeding  $T_A$ . Even at low temperature, when the maximum field of opposite polarity visited by the sample ( $B_{\text{max}}$ ) is sufficiently small, the hysteresis has a bow-tie shape<sup>24</sup>. Not only the shape of the loop but also other features such as the threshold field for flipping spins ( $B_0$ ) and the asymmetry between opposite field polarities ( $B_{0+} \neq B_{0-}$ ), the exchange bias, depend on  $B_{\text{max}}$ . Thus, the system has a memory of the previously visited  $B_{\text{max}}$ . We identify a distinct small spin population as the driver of this memory. They keep their polarity even when the magnetic field is almost an order of magnitude larger than the coercive field for most (>99%) of the spin population. A detailed study of this memory effect

leads us to conclude that  $T_A$  is not a thermodynamic phase transition, but a crossing point between boundaries in the (temperature, field) plane. One boundary separates memory-less and memory-full regimes. The other frontier determines the shape of the hysteresis loop and multiplicity of domains. When a single-domain state is abruptly replaced by a single-domain state of opposite polarity, the loop has a rectangular shape. A bow-tie shape emerges when the reversal has a multi-domain interlude. The existence of more than one type of ordered spins may be due to bulk/surface dichotomy<sup>23</sup>. Finally, by performing local magnetometry studied with miniature Hall probes, we show that when magnetization is not uniform, features associated with thermodynamics of small systems may emerge at length scales as large as a few microns.

## Results

Figure 1b shows the temperature dependence of magnetization in one of our samples. Magnetization is enhanced below the Curie temperature of 175 K and saturates to 0.3 Bohr magneton,  $\mu_B$ , per Co atom at low temperatures. Inside the ferromagnetic state, an anomaly and a hysteresis in temperature are detectable, which both disappear when the applied magnetic field becomes large enough to saturate magnetization.

#### **Magnetization hysteresis loops**

Figure 2a–f shows the evolution of the magnetization hysteresis loop as a function of temperature in a  $\text{Co}_3\text{Sn}_2\text{S}_2$  single crystal. These loops were obtained by sweeping the field between -0.5 T and +0.5 T, corresponding to  $B_{\text{max}}=0.5$  T. At low temperatures (Fig. 2a–c), the hysteresis loop looks like a rectangle as in a hard magnet. The magnetic field suddenly flips all spins at well-defined thresholds identified as  $B_{0+}$  and  $B_{0-}$ . Let us define  $B_0=(B_{0+}-B_{0-})/2$ , the average spin-flip field. At T > 120 K (Fig. 2d–f,) the hysteresis loop is no more rectangular. This implies that all spins do not flip at  $B=B_{0\pm}$ . The jump in magnetization is followed by a smooth and almost field-linear variation of magnetization. This is the 'bow-tie' hysteresis shape<sup>21</sup>.

The evolution seen in Fig. 2a–f is similar to what was reported by Lachman et al. 21, who found that the hysteresis loop acquires a 'bow-tie' shape above a threshold temperature. The only difference is that our threshold temperature ( $T_A = 115 \text{ K} \pm 5 \text{ K}$ ) is lower than theirs ( $T_G = 125 \text{ K}$ ). This difference will be explained at the end of this paper. Another feature which appears at low temperature is a genuine asymmetry between positive and negative orientations :  $B_{0+} \neq B_{0-}^{21}$ , which is particularly visible in Fig. 2h.

Panels g-l in figure 2 show the hysteresis loops at 10 K with different maximum sweeping fields,  $B_{\rm max}$ . The evolution is similar to the one induced by warming. When  $B_{\rm max}=5\,{\rm T}$ , the magnetization loop is rectangular. Decreasing  $B_{\rm max}$  reduces  $B_0$ , in agreement with what was previously reported<sup>24</sup>. For sufficiently small  $B_{\rm max}$  (that is, when  $B_{\rm max}<0.35\,{\rm T}$ ), the hysteresis loop acquires a bow-tie shape. The emergence of bow-tie shape and low values of  $B_0$  are concomitant. We refer to the amplitude of  $B_0$  below which the hysteresis loop displays a bow-tie feature as  $B_0^{\rm ht}$ .

Thus, at low temperature, the shape of the hysteresis loop and the amplitude of  $B_0$  both depend on  $B_{\rm max}$ . In other words, the amplitude of magnetization at a given magnetic field does not exclusively depend on temperature and magnetic field, but also on the magnetic field applied in the past. If the latter is not large enough, a memory persists. Memory formation in condensed matter is defined as an 'ability to encode, access, and erase signatures of past history in the state of a system'<sup>29</sup>. The present case is reminiscent of another topological magnet, namely  $Mn_3X$  (either with  $X=Sn^{30}$  or  $X=Ge^{31}$ ). However, as we will see below, here the information is stocked not in the domain walls between antiferromagnetic domains, but in a secondary spin population.

#### Origin of the Bow-tie shape

Multiplicity of magnetic domains in  $\text{Co}_3\text{Sn}_2\text{S}_2$ , which occurs when the amplitude of magnetization is below its peak value of  $M_s \simeq 0.3 \,\mu_B/\text{Co}$ , has

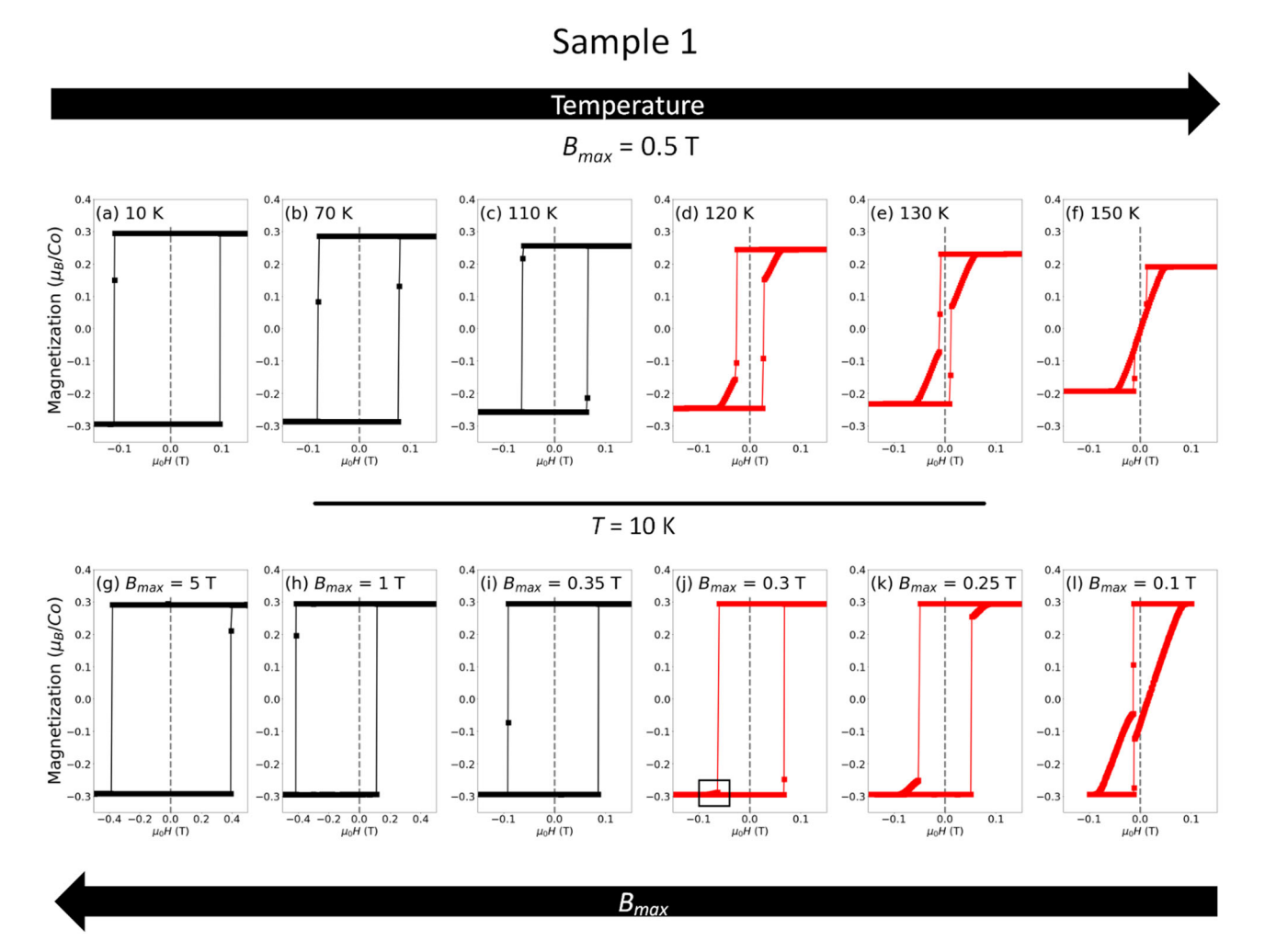


**Fig. 2** | **Shape of the magnetization hysteresis loops.** a–f Hysteresis loops at 10 K, 70 K,110 K, 120 K, 130 K, 150 K, all with an identical maximum sweeping magnetic field ( $B_{\rm max}=0.5$  T). Note the emergence of a bow-tie feature above 120 K.

**g–l** Hysteresis loops at T = 10 K with different maximums sweeping fields ( $B_{\rm max}$  = 5 T, 1 T, 0.35 T, 0.3 T, 0.25 T and 0.1 T). When  $B_{\rm max}$  becomes smaller than 0.35 T, a bow-tie feature emerges.

been probed by microscopic techniques <sup>17,32,33</sup>. To identify the origin of  $B_0^{bt}$  and the change in the shape of the hysteresis loop across this threshold, we scrutinized hysteresis loops with a very small (< 0.2 T)  $B_{\rm max}$  leading to a magnetization lower than  $M_s$ .

Figure 3a illustrates the variation of magnetization with applied magnetic field during three successive hysteresis loops where the amplitude of  $B_{\rm max}$  is incrementally reduced after each loop. The first two loops (blue and green) have a bow-tie shape: magnetization is first flat, then abruptly drops (or jumps) and then shows a steady drift towards its saturated value with a slope tending to be independent of  $B_{\rm max}$ . During this steady drift, the system hosts multiple magnetic domains. In the third loop (red),  $B_{\rm max}$  is so low that abrupt jumps (or drops) vanish. Note that the slope of magnetization in the red loop is similar to the slope of magnetization in the green and blue loops which presents a bow-tie shape. This slope, which does not depend on  $B_{\rm max}$ , sets  $B_0^{bt}$ . Dividing  $\mu_0 M_s$  by dM/dH yields 85 mT (Fig. 3a), close to the threshold  $B_0^{bt}$  revealed in the transition between panels i and j of Fig. 2.

Magnetization loops for a thicker sample (Fig. 3b) are similar, but there is a quantitative difference. The magnetization slope is steeper in the thicker sample, which has almost a cubic shape.  $M_s$  is identical in the two samples and therefore the threshold field is reduced to 39 mT in this thicker sample. Thus, with increasing thickness, the multi-domain window becomes narrower, the magnetization slope becomes steeper and  $B_0^{bt}$  is reduced.

The difference in the demagnetizing factors of the two samples provides a quantitative account of this thickness dependence. As seen in Table 1, D, the demagnetizing factor calculated by using the formula for a rectangular prism<sup>34</sup>, is very close to  $\frac{dH}{dM}$ , the inverse of the magnetization slope measured in the experiment.

When the magnetic field becomes equal to  $B_{0\pm}$ , an energy barrier is crossed and spins flip to the opposite orientation. If  $|B_{0\pm}| \geqslant \mu_0 DM_s$ , the spin-flip is total and the loop is rectangular. On the other hand, if  $|B_{0\pm}| \leqslant \mu_0 DM_s$ , spin-flip is partial and the loop has a bow-tie shape, because a multi-domain configuration is stable thanks to the demagnetization energy. This leads us to  $B_0^{bt} = \mu_0 DM_s$ , in agreement with the experimental observation.

## Temperature dependence of the memory effect

We saw that the magnitude of  $B_0$  depends on the maximum sweeping field,  $B_{\max}$ . Figure 3c illustrates this dependence for different temperatures in a semi-log plot. At each temperature, the initial increase  $B_0$ , which is roughly linear in  $B_{\max}$  ends by saturation to a constant value, which we dub  $B_0^\star$ . Let us call  $B_{\max}^\star$  the magnitude of  $B_{\max}$  above which  $B_0 = B_0^\star$ . As one can see in the figure, both  $B_0^\star$  and  $B_{\max}^\star$  steadily decrease with increasing temperature. The picture drawn by this data is following: when  $B_{\max} < B_{\max}^\star$ , the system has a memory, which shows itself in the magnitude of  $B_0$ . Spin flip occurs at a threshold magnetic field, which depends on the previously visited field. When  $B_{\max} > B_{\max}^\star$ , there is no such memory and  $B_0(T) = B_0^\star(T)$  is independent of previous history.

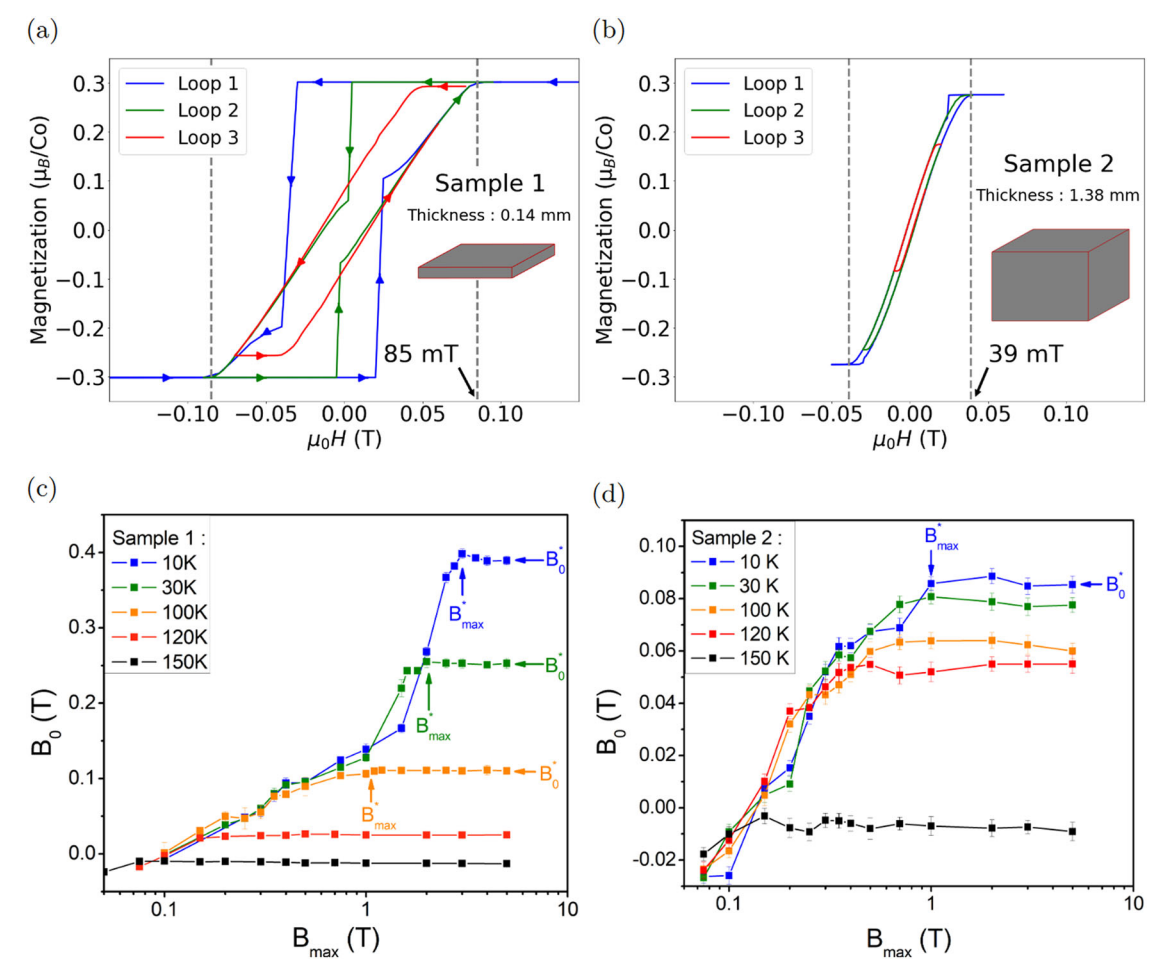


Fig. 3 | Magnetization loops for small  $B_{\rm max}$  and  $B_{\rm max}$  dependence of  $B_0$ . a Three Magnetization loops at 10 K. Loop 1 (blue): starting field at 0.2 T. Loop 2 (green): starting field at 0.1 T. Loop 3 (red): starting field at 0.08 T. b Loops for a thicker sample. Loop 1 (blue): starting field at 0.06 T. Loop 2 (green): starting field at 0.04 T. Loop 3 (red): starting field at 0.02 T. Bow-tie features tend to two parallel lines.  $\mathbf{c}$   $B_0$  as

function of  $B_{\max}$  at different temperatures for sample 1; **d** Same for sample 2. At each temperature,  $B_0$  initially increases linearly with increasing  $B_{\max}$ . It eventually saturates to a constant value. This threshold sweeping field,  $B_{\max}^*$ , is shown by arrows. The saturated amplitude of  $B_0$ , called  $B_0^*$  is also shown. Both  $B_0^*$  and  $B_{\max}^*$  decrease with increasing temperature.

Table 1 | Samples dimensions and aspect ratio

	Dimensions (mm³)	Aspect ratio	D	dH/dM
Sample 1	$1.21 \times 0.89 \times 0.14$	0.13	0.76	0.69
Sample 2	1.93 × 1.20 × 1.38	0.88	0.35	0.38

For both samples, the calculated demagnetizing factor, D, is close to the measured dH/dM (the inverse of the magnetization slope) when  $B < B_0^{\rm ht}$  implying  $B_0^{\rm ht} = \mu_0 {\rm DM_s}$ .

Figure 3d presents the same data for the thicker sample (#2). The behavior is qualitatively similar: After an initial increase,  $B_0$  saturates at a temperature dependent magnitude. Note, however, that the absolute value of  $B_0^\star$  is much smaller in the thicker sample. At low temperature,  $B_0^\star \simeq 0.4~\mathrm{T}$  in sample 1 and  $B_0^\star \simeq 0.09~\mathrm{T}$  in sample 2. It is noteworthy that, for both samples,  $B_{\mathrm{max}}^\star/B_0^\star \approx 8$  and this ratio does not show any strong temperature dependence. This indicates that the temperature-induced decrease in both field scales is similar.

 $B_0^{\star}$  is the coercive field of the system when the memory is erased. As expected<sup>35</sup>, it decreases with increasing temperature. Its amplitude in the zero-temperature limit is much smaller than the magneto-crystalline anisotropy field, i.e. to the in-plane magnetic field needed to saturate magnetization. The latter is as large as ~23 T<sup>36</sup>. This difference makes Co<sub>3</sub>Sn<sub>2</sub>S<sub>2</sub> another example of what is known as 'Brown's coercivity paradox'<sup>37</sup>. Experiments have found that the coercivity is often much smaller than the

lowest bound expected according to the magneto-crystalline anisotropy<sup>38</sup>. It has been shown that large demagnetizing fields developed near sharp corners play a significant role in setting coercivity<sup>37</sup> and imperfections can reduce the expected coercive field<sup>39</sup>.

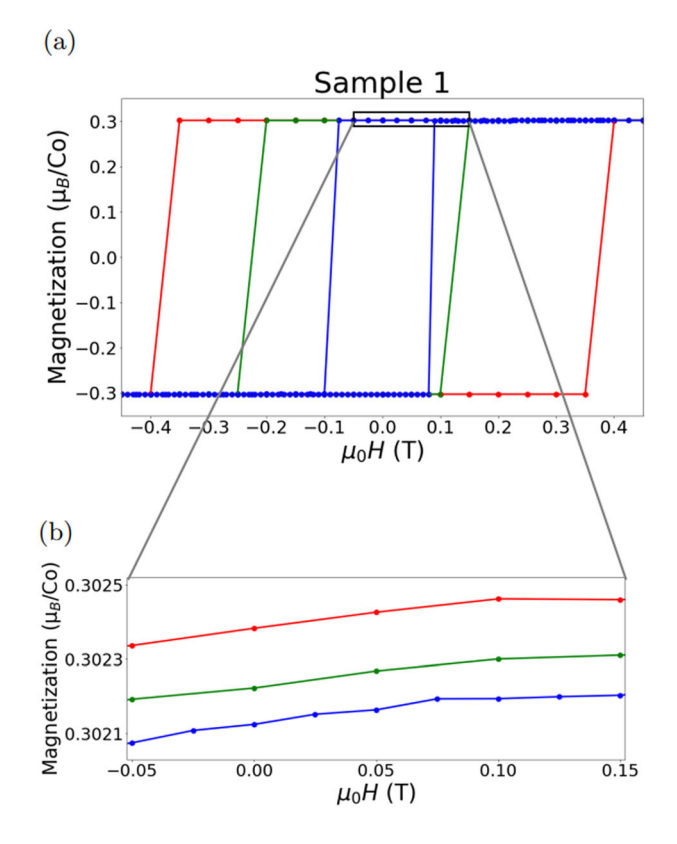
Thus, when the maximum sweeping field  $B_{\rm max}$  becomes lower than a threshold  $(B_{\rm max}^{\star})$ ,  $B_0$  becomes lower than its peak value  $B_0^{\star} \simeq 0.4$  T. Moreover, this is also the case of the difference between  $|B_{0+}|$  and  $|B_{0-}|$ , which becomes significantly larger than our experimental margin. Thus, the memory effect tunes the exchange bias, too (See the Supplementary Materials for details  $^{40}$ ).

#### Zooming on saturated magnetization

Given the content of this memory, one may suspect that when it is not erased, the energy barrier between two single-domain states is attenuated. This may be caused by the presence of a secondary spin component or population which modifies the overall energy landscape and attenuates the height of the barrier. A careful examination of saturated magnetization at the end of a hysteresis loop confirms this.

Figure 4a displays three loops all at 10 K with three different endings ( $B_{\rm max}$ = 0.5 T; 1.5 T and 4.8 T). The figure shows that  $B_0$  increases with increasing  $B_{\rm max}$ , as we saw above. At first sight, magnetization appears to saturate at the same amplitude. However, this is not the case. Figure 4b is a zoom on the three curves near the maximum magnetization. One can see that there is a small, yet finite difference between the three curves. With

increasing  $B_{\rm max}$  the amplitude of magnetization at the end of a 'rectangular' loop is larger. We carefully documented the dependence of spontaneous magnetization at the end of a loop (measured at  $B=\pm\,0.05\,{\rm T}$ ) on the amplitude of the sweeping magnetic field.



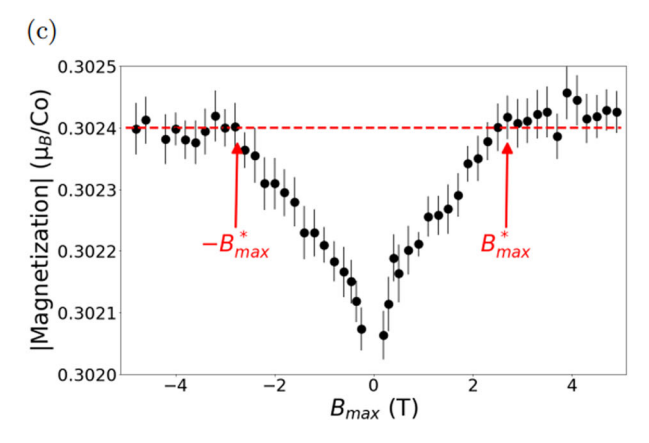


**Fig. 4** | **Memory effect in "saturated" magnetization, at 10 K. a** Three magnetization loops, red:  $B_{\text{max}} = 4.8 \text{ T}$ , green:  $B_{\text{max}} = 1.5 \text{ T}$  and blue:  $B_{\text{max}} = 0.5 \text{ T}$ . **b** Zoom in positive magnetization at low field. **c**  $B_{\text{max}}$  dependence of the absolute value of magnetization at  $\pm$  50 mT (depending on  $B_{\text{max}}$  sign).

Figure 4c shows the result. The spontaneous magnetization at the end of a loop increases with increasing  $|B_{\text{max}}|$  before saturating to a constant value when  $B_{\text{max}}$  becomes equal to  $B_{\text{max}}^{\star}$ . The detected increase of magnetization between  $B_0^{\star}$  (the end of the loop) and its eventual saturation above  $B_{\max}^{\star}$  is tiny ( $\approx 0.1\%$ ), but larger than our experimental margin. This observation has an important implication: when the sample has not visited a sufficiently large  $B_{\text{max}}$ , it hosts a small population of spins whose magnetization does not correspond to the polarity of majority spins. This population is where the memory is stored. The existence of a  $B_{\text{max}}^{\star}$  (roughly 8 times larger than  $B_0^*$ ) is caused by this secondary spin population whose coercive field is larger and much more broadly distributed than the coercive field of the majority spins. The secondary spins, presumably three orders of magnitude more dilute than the principal population, may be situated either at the surface of the sample or at offstoichiometric sites.

#### Discussion

Having identified four different field scales (See Table 2), let us now turn our attention to the phase diagram.

# Origin of $T_A$ , the additional temperature scale

Figure 5a shows the evolution of  $B_0^\star$  and  $B_0^{bt}$  with temperature.  $B_0^{bt}$ , the threshold field for bow-tie shape, is almost flat and its absolute value coincides with  $\mu_0 D M_s$ . In contrast,  $B_0^\star$ , the saturated  $B_0$ , is temperature dependent and rapidly decreases with increasing temperature.  $T_A$  is the temperature at which  $B_0^\star$  and  $B_0^{bt}$  cross each other. When  $B_0^\star$  falls below  $B_0^{bt}$ , whatever the sweeping field  $B_{\max}$ , one finds  $B_0 < B_0^{bt}$ . This makes a bow-tie shape unavoidable. Thus, no thermodynamic phase transition occurs at  $T_A$ . This temperature threshold arises as a result of the crossing between two boundaries.

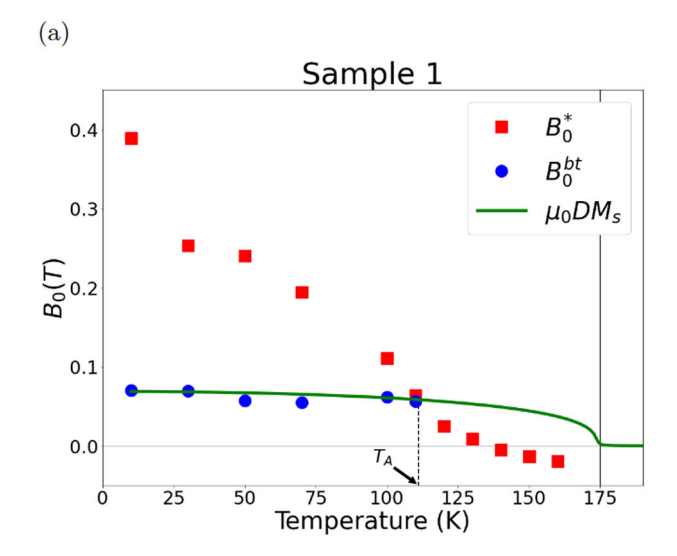
This is further illustrated in Fig. 5b, a representation of the evolution of  $B_{\max}^{\star}$  and  $B_{\max}^{bt}$  in the (field, temperature) plane. When  $B_{\max} > B_{\max}^{\star}$ , the system has no memory (that is, the shape of hysteresis loop does not depend on the past history) and when  $B_{\max} < B_{\max}^{\star}$ , there is a memory.  $B_{\max}^{\star}(T)$  is the boundary between two states with and without memory. A second boundary is defined by  $B_{\max}^{bt}$ . When  $B_{\max}$  is larger than this threshold, the hysteresis loop is rectangular. Since  $B_{\max}/B_0$  ratio does not change with temperature,  $T_A$ , the temperature at which  $B_{\max}^{bt} = B_{\max}^{\star}$  is similar to what can be seen in Fig. 5a. Since  $B_0^{bt}$  and  $B_{\max}^{bt}$  depend on the demagnetizing factor and the sample morphology, the horizontal lines in these figures are expected to vary from sample to sample with the change in the aspect ratio. This would explain the fact that the reported secondary temperature differs from one study to another.

Thus, the magnetic order in  $\text{Co}_3\text{Sn}_2\text{S}_2$  remains ferromagnetic with spins oriented along the c-axis. However, in presence of a magnetic field oriented along the c-axis, as a function of temperature and magnetic field (both at present and in the past), multiple meta-stable configurations can arise. What distinguishes them is the polarity in different sub-sets of spin population, despite the global ferromagnetic order.

Table 2 | Four distinct field scales identified in this study

Field scale	Amplitude (T)	Definition
$B_0^{\star}$ (T)	0.4	Spin-flip field in absence of memory (coercivity of main spin population)
$B_{\max}^{\star}$ (T)	3	Sweeping field above which no memory persists (maximum coercivity of secondary spin population)
$B_0^{bt}$ (T)	0.085	Hysteresis becomes bow-tie when the spin-flip field falls below this threshold
$B_{\max}^{bt}$ (T)	0.35	Hysteresis becomes bow-tie when the magnetic field is swept below this threshold

The amplitudes are given for sample 1 at T = 10 K.  $B_0^*$  and  $B_0^{bt}$  refer to spin-flip fields, at which the magnetic field shows an abrupt jump.  $B_{\text{max}}^{bt}$  and  $B_{\text{max}}^*$  refer to maximum sweeping field tuning the spin-flip field,  $B_0$ .  $B_0^{bt}$  and  $B_{\text{max}}^{bt}$  depend on the demagnetizing factor and show little dependence on temperature.  $B_{\text{max}}^*$  and  $B_0^*$  both decrease with warming.



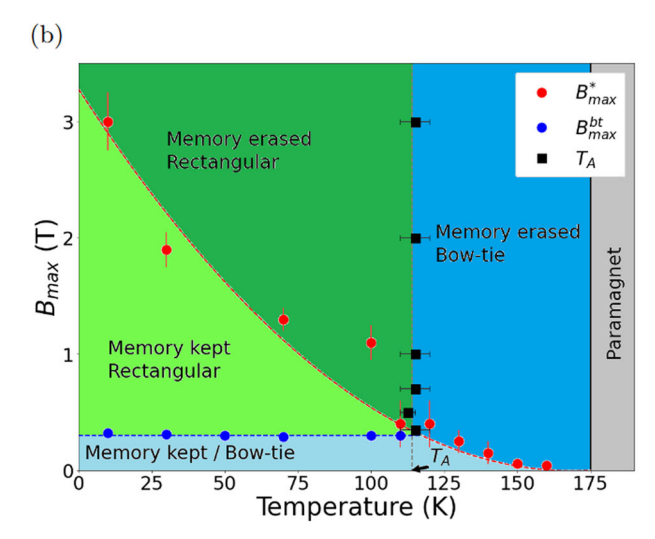


Fig. 5 | Field scales in magnetization loops. a  $B_0^*$  and  $B_0^{bt}$  versus temperature. The measured  $B_0^{bt}$  tracks  $\mu_0 D M_s$  (with D=0.76), which is represented by the green solid line.  $B_0^*$  and  $B_0^{bt}$  cross each other at  $T_A$ . Above this, hysteresis loops can only have a bow-tie shape for whatever  $B_{\rm max}$  because of the  $B_0^* < B_0^{bt}$  inequality. b  $B_{\rm max}^*$  and  $B_{\rm max}^{bt}$  versus temperature. Dashed lines are guides to the eye.  $T_A=115\pm 5$  K, corresponds to the crossing point of  $B_{\rm max}^*$  and  $B_{\rm max}^{bt}$ .

## Thermodynamic limit for well-defined magnetization

One manifestation of this meta-stability is the contrast between local and global magnetization, shown in Fig. 6. When the system is in the rectangular regime, local magnetization, measured with micron-sized Hall sensors (see supplementary material for details<sup>40</sup>), is very similar to the magnetization of the whole sample. In other words, the passage between single-domain regimes of opposite polarities is almost identical everywhere in the sample (Fig. 6a, b). On the other hand, when the sample is multi-domain, while global magnetization presents a smooth and reproducible slope (Fig. 6c), local magnetization is not reproducible from one sweep to another (Fig. 6d). This confirms that when the memory is not erased, the energy landscape is not smooth<sup>41</sup>. There are numerous competing spin configurations, spatially distinct over a micrometer, but with similar global magnetization. Our case emerges as a platform for studying thermodynamics of small systems<sup>42</sup>.

## Possibly related phenomena in other magnetic solids

Let us note that  $Co_3Sn_2S_2$  is not the first case of multiple spin populations. In  $SrRuO_3$  thin films <sup>43,44</sup> with a thickness of few unit cells, there is an additional

peak in the Hall response. It has been proposed that it is caused by contributions of opposite signs from two distinct magnetic regions with different saturation magnetizations  $^{45}$ . The two contributions have different coercive fields, but this difference is far below the order of magnitude difference we see in our case. A similar observation has been reported in NiCo<sub>2</sub>O<sub>3</sub> thin films  $^{46}$ .

These observations indicate that the existence of distinct spin populations with different coercive fields in a magnet may be more common than previously thought.

In summary, we investigated the evolution of the magnetization hysteresis loop in  $\text{Co}_3\text{Sn}_2\text{S}_2$  with temperature and with the maximum swept magnetic field,  $B_{\text{max}}$ . We found that, at each temperature, increasing  $B_{\text{max}}$  leads to an enhancement of the coercive field up to a saturation value,  $B_{\text{max}}^{\star}$ . In addition, the amplitude of the saturated magnetization displays a small, yet significant, dependence on  $B_{\text{max}}$ . This suggests the presence of a small secondary spin population with a coercive field larger than that of the main population. The memory of the last  $B_{\text{max}}$  is stored by this minority spins, which do not flip if the sweeping field is lower than  $B_{\text{max}}^{\star}$ .

A temperature scale,  $T_A$ , distinct from the Curie temperature, was identified by several previous studies. It was suggested that it corresponds to a thermodynamic phase transition within the magnetically ordered state. This secondary phase was suggested to be in-plane antiferromagnetism<sup>15</sup>, spin glass<sup>21</sup> or an anomaly in domain wall mobility<sup>17</sup>. According to our study,  $T_A$  does not correspond to a thermodynamic phase transition, but to a crossing point between meta-stable states. The two boundaries which cross at  $T_A$  separate regimes with and without memory and regimes which are single-domain and multiple-domain. The origin of the two distinct coercive fields corresponding to two distinct spin populations emerges as a puzzle to be addressed by future studies.

#### Methods

Crystals of  $\text{Co}_3\text{Sn}_2\text{S}_2$  were grown by self-flux method as detailed previously.

Magnetization was measured using a Quantum Design MPMS in Vibrating Sample Magnetometer (VSM) mode with magnetic field applied along the crystalline c-axis with a quartz sample holder.

The hysteresis loops displayed in Figs. 2 and 3c, d, were obtained according to the following protocol:

- Set the temperature.
- Reduce the remanent field by sweeping the applied field with gradually decreasing  $|B_{\rm max}|$  until finding that magnetization is not saturated anymore. For instance, the field was swept first from -0.5 T, to 0.2 T then to -0.1 T, then to 0.05 T, and finally to 0 T.
- Loops were measured consecutively, starting from the smallest to the largest B<sub>max</sub> without additional delay between steps of measurement.
- Loops measurement were done by initially setting the external field to  $B_{\rm max}$  (with a sweep rate of 100 Oe/s). Then the external field was swept at 10 Oe/s in linear mode from  $B_{\rm max}$  to  $-B_{\rm max}$ , then swept back to  $B_{\rm max}$ .

Loops in figure 4 were obtained by decreasing  $B_{\rm max}$ . They are similar to experiments performed by increasing  $B_{\rm max}$ .

To measure local magnetization, we employed an array of Hall sensors based on high-mobility AlGaAs/GaAs heterostructure with a 160 nm two-dimensional electron gas (2DEG) below the surface, as done before  $^{30,47,48}$ . The device was fabricated using electron beam lithography and 250 V argon ions to define the mesa. The device consists of ten  $5\times 5\,\mu\text{m}^2$  sensors separated from their neighbor by  $100\,\mu\text{m}$ . The hall resistance of the sensors are  $R_{Hall}\approx 6.2\times 10^3*B$ . The local magnetic field at the surface of the sample was obtained by measuring the Hall resistivity of a sensor put on the sample. The sensor resistivity was measured using a Quantum Design PPMS with applied field along the c-axis of the sample.

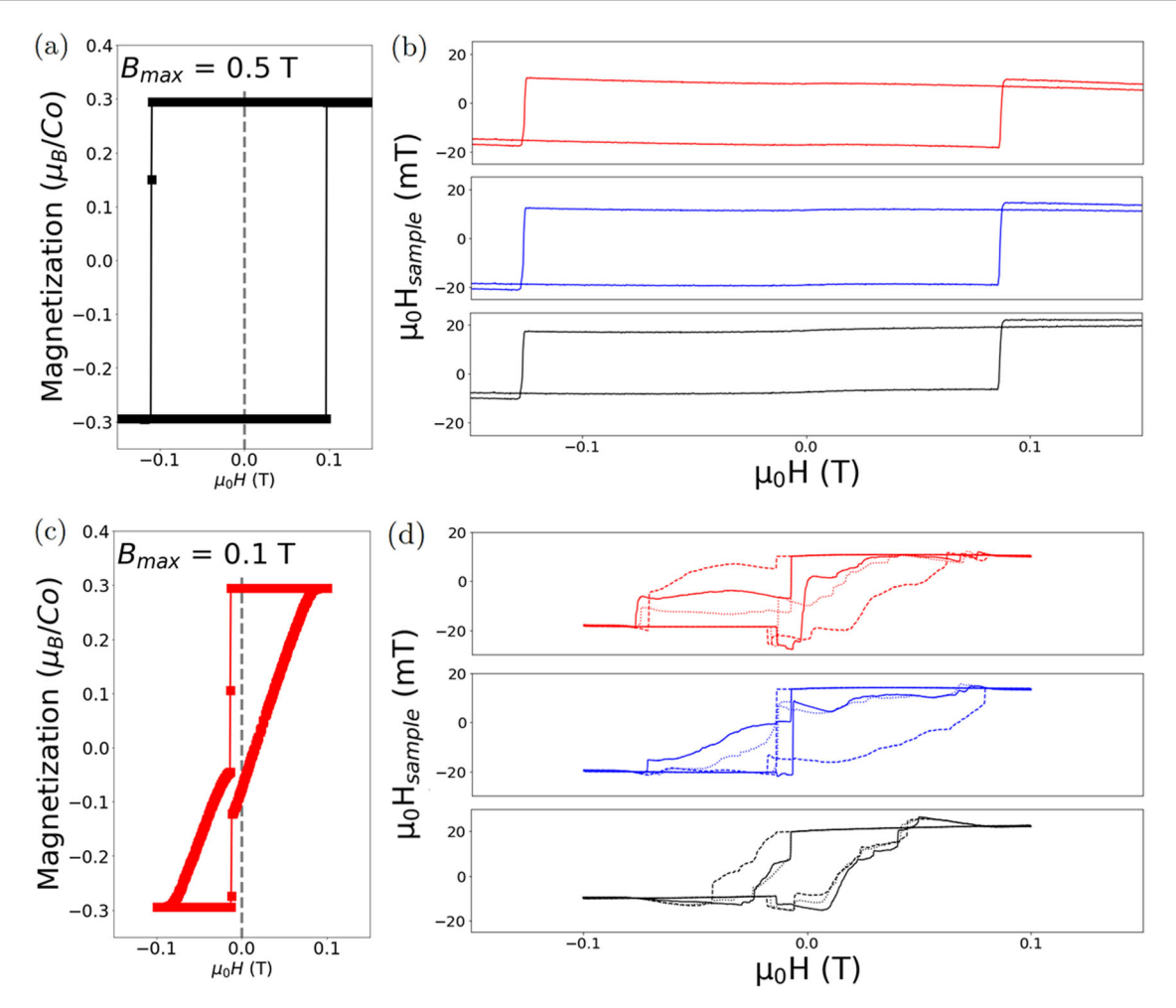


**Fig. 6 | Local and global magnetization. a** Magnetization of the whole sample, measured with a vibrating-sample magnetometer, at 10 K for  $B_{\rm max}$  = 0.5 T. **b** Local magnetization, measured in identical conditions by an array of 2DEG micron-sizes Hall sensors put on the surface of the sample. The three curves represent the local

magnetic field at three different positions of the sample. c Magnetization of the whole sample at 10 K for  $B_{\rm max}=0.1$  T. Hysteresis displays a bow-tie shape. d Local magnetization measured in similar conditions. Each color represents a position on the sample (three consecutive hysteresis loops were measured.).

# **Data availability**

The data that support the findings of this study are available from the corresponding authors upon reasonable request.

Received: 16 July 2024; Accepted: 24 January 2025; Published online: 19 February 2025

# References

- Zabel, M., Wandinger, S. & Range, K.-J. Ternary Chalcogenides M<sub>3</sub>M<sub>2</sub>X<sub>2</sub> with Shandite-Type Structure. *Z. f.ür. Naturforsch. B* 34, 238–241 (1979).
- Liu, E. et al. Giant anomalous Hall effect in a ferromagnetic kagomelattice semimetal. Nat. Phys. 14, 1125–1131 (2018).
- Wang, Q. et al. Large intrinsic anomalous Hall effect in half-metallic ferromagnet Co<sub>3</sub>Sn<sub>2</sub>S<sub>2</sub> with magnetic Weyl fermions. *Nat. Commun.* 9, 3681 (2018).
- 4. Vaqueiro, P. & Sobany, G. G. A powder neutron diffraction study of the metallic ferromagnet Co<sub>3</sub>Sn<sub>2</sub>S<sub>2</sub>. *Solid State Sci.* **11**, 513–518 (2009).
- Dedkov, Y. S., Holder, M., Molodtsov, S. L. & Rosner, H. Electronic structure of shandite Co<sub>3</sub>Sn<sub>2</sub>S<sub>2</sub>. J. Phys.: Conf. Ser. 100, 072011 (2008).
- Holder, M. et al. Photoemission study of electronic structure of the half-metallic ferromagnet Co<sub>3</sub>Sn<sub>2</sub>S<sub>2</sub>. Phys. Rev. B 79, 205116 (2009).
- Schnelle, W. et al. Ferromagnetic ordering and half-metallic state of Sn<sub>2</sub>Co<sub>3</sub>S<sub>2</sub> with the shandite-type structure. *Phys. Rev. B* 88, 144404 (2013).

- 8. Ding, L. et al. Intrinsic anomalous Nernst effect amplified by disorder in a half-metallic semimetal. *Phys. Rev. X* **9**, 041061 (2019).
- Ding, L. et al. Quantum oscillations, magnetic breakdown and thermal Hall effect in Co<sub>3</sub>Sn<sub>2</sub>S<sub>2</sub>. J. Phys. D: Appl. Phys. 54, 454003 (2021).
- Sakai, A. et al. Giant anomalous Nernst effect and quantum-critical scaling in a ferromagnetic semimetal. *Nat. Phys.* 14, 1119–1124 (2018).
- Li, X. et al. Anomalous Nernst and Righi-Leduc effects in Mn<sub>3</sub>Sn: Berry curvature and entropy flow. *Phys. Rev. Lett.* 119, 056601 (2017).
- 12. Ikhlas, M. et al. Large anomalous Nernst effect at room temperature in a chiral antiferromagnet. *Nat. Phys.* **13**, 1085–1090 (2017).
- 13. Xu, L. et al. Finite-temperature violation of the anomalous transverse Wiedemann-Franz law. Sci. Adv. 6, eaaz3522 (2020).
- 14. Ren, Z. et al. Plethora of tunable weyl fermions in kagome magnet Fe<sub>3</sub>Sn<sub>2</sub> thin films. *npj Quantum Mater.* **7**, 109 (2022).
- 15. Guguchia, Z. et al. Tunable anomalous hall conductivity through volume-wise magnetic competition in a topological kagome magnet. *Nat. Commun.* **11**, 559 (2020).
- Zhang, Q. et al. Unusual Exchange Couplings and Intermediate Temperature Weyl State in Co<sub>3</sub>Sn<sub>2</sub>S<sub>2</sub>. Phys. Rev. Lett. 127, 117201 (2021).
- Lee, C. et al. Observation of a phase transition within the domain walls of ferromagnetic Co<sub>3</sub>Sn<sub>2</sub>S<sub>2</sub>. Nat. Commun. 13, 3000 (2022).
- Soh, J.-R. et al. Magnetic structure of the topological semimetal Co<sub>3</sub>Sn<sub>2</sub>S<sub>2</sub>. Phys. Rev. B 105, 094435 (2022).

- Neubauer, K. J. et al. Spin structure and dynamics of the topological semimetal Co<sub>3</sub>Sn<sub>2-x</sub>ln x S<sub>2</sub>. npj Quantum Mater. 7, 112 (2022).
- Kassem, M. A., Tabata, Y., Waki, T. & Nakamura, H. Low-field anomalous magnetic phase in the kagome-lattice shandite Co<sub>3</sub>Sn<sub>2</sub>S<sub>2</sub>. *Phys. Rev. B* 96, 014429 (2017).
- Lachman, E. et al. Exchange biased anomalous Hall effect driven by frustration in a magnetic kagome lattice. *Nat. Commun.* 11, 560 (2020).
- Živković, I. et al. Unraveling the origin of the peculiar transition in the magnetically ordered phase of the Weyl semimetal Co<sub>3</sub>Sn<sub>2</sub>S<sub>2</sub>. Phys. Rev. B 106, L180403 (2022).
- Avakyants, A., Orlova, N., Timonina, A., Kolesnikov, N. & Deviatov, E. Evidence for surface spin structures from first order reversal curves in Co<sub>3</sub>Sn<sub>2</sub>S<sub>2</sub> and Fe<sub>3</sub>GeTe<sub>2</sub> magnetic topological semimetals. *J. Magn. Magn. Mater.* 573, 170668 (2023).
- Noah, A. et al. Tunable exchange bias in the magnetic Weyl semimetal Co<sub>3</sub>Sn<sub>2</sub>S<sub>2</sub>. Phys. Rev. B 105, 144423 (2022).
- Shen, Z., Zhu, X., Ullah, R. R., Klavins, P. & Taufour, V. Anomalous depinning of magnetic domain walls within the ferromagnetic phase of the Weyl semimetal Co<sub>3</sub>Sn<sub>2</sub>S<sub>2</sub>. *J. Phys.: Condens. Matter* 35, 045802 (2022).
- Zhang, Q. et al. Hidden local symmetry breaking in a kagome-lattice magnetic Weyl semimetal. *J. Am. Chem. Soc.* 144, 14339–14350 (2022).
- Stamps, R. L. Mechanisms for exchange bias. J. Phys. D: Appl. Phys. 33, R247 (2000).
- Pate, S. E. et al. Field orientation dependent magnetic phases in the weyl semimetal Co<sub>3</sub>Sn<sub>2</sub>S<sub>2</sub>. Phys. Rev. B 108, L100408 (2023).
- Keim, N. C., Paulsen, J. D., Zeravcic, Z., Sastry, S. & Nagel, S. R. Memory formation in matter. Rev. Mod. Phys. 91, 035002 (2019).
- Li, X. et al. Chiral domain walls of Mn<sub>3</sub>Sn and their memory. Nat. Commun. 10, 3021 (2019).
- 31. Xu, L., Li, X., Ding, L., Behnia, K. & Zhu, Z. Planar Hall effect caused by the memory of antiferromagnetic domain walls in Mn<sub>3</sub>Ge. *Appl. Phys. Lett.* **117**, 222403 (2020).
- Sugawara, A. et al. Magnetic domain structure within half-metallic ferromagnetic kagome compound Co<sub>3</sub>Sn<sub>2</sub>S<sub>2</sub>. Phys. Rev. Mater. 3, 104421 (2019).
- Howlader, S., Ramachandran, R., Singh, Y. & Sheet, G. et al. Domain structure evolution in the ferromagnetic Kagome-lattice Weyl semimetal Co<sub>3</sub>Sn<sub>2</sub>S<sub>2</sub>. J. Phys.: Condens. Matter 33, 075801 (2020).
- Aharoni, A. Demagnetizing factors for rectangular ferromagnetic prisms. J. Appl. Phys. 83, 3432–3434 (1998).
- Garcia-Otero, J., Garcia-Bastida, A. & Rivas, J. Influence of temperature on the coercive field of non-interacting fine magnetic particles. J. Magn. Magn. Mater. 189, 377–383 (1998).
- Shen, J. et al. On the anisotropies of magnetization and electronic transport of magnetic Weyl semimetal Co<sub>3</sub>Sn<sub>2</sub>S<sub>2</sub>. Appl. Phys. Lett. 115, 212403 (2019).
- 37. Hartmann, U. Origin of Brown's coercive paradox in perfect ferromagnetic crystals. *Phys. Rev. B* **36**, 2331 (1987).
- 38. Coey, J. M. Magnetism and magnetic materials (Cambridge university press, 2010).
- Aharoni, A. Reduction in coercive force caused by a certain type of imperfection. *Phys. Rev.* 119, 127 (1960).
- 40. See Supplemental Material for more details (2024).
- 41. Wales, D. J. *Energy Landscapes* (pp. 437–507. Springer Berlin Heidelberg, Berlin, Heidelberg, 2001).
- Hill, T. Thermodynamics of Small Systems. Dover Books on Chemistry https://books.google.fr/books?id=Xa-yAAAAQBAJ (Dover Publications, 1994).

- 43. Ding, Z. et al. Magnetism and berry phase manipulation in an emergent structure of perovskite ruthenate by (111) strain engineering. *npj Quantum Mater.* **8.** 43 (2023).
- 44. Kar, U. et al. The thickness dependence of quantum oscillations in ferromagnetic Weyl metal SrRuO<sub>3</sub>. npj Quantum Mater. **8**, 8 (2023).
- Kimbell, G. et al. Two-channel anomalous Hall effect in SrRuO<sub>3</sub>. Phys. Rev. Mater. 4, 054414 (2020).
- Zhou, G. et al. Observation of two-channel anomalous Hall effect in perpendicularly magnetized NiCo<sub>2</sub>O<sub>4</sub> epitaxial films. *Phys. Rev. B* 108, 094442 (2023).
- Collignon, C. et al. Superfluid density and carrier concentration across a superconducting dome: The case of strontium titanate. *Phys. Rev. B* 96, 224506 (2017).
- Behnia, K., Capan, C., Mailly, D. & Etienne, B. Internal avalanches in a pile of superconducting vortices. *Phys. Rev. B* 61, R3815–R3818 (2000).

## **Acknowledgements**

This study was supported by Jeunes Equipes de l'Institut de Physique du Collège de France, and by a grant attributed by the lle de France regional council. C.M. acknowledges a PhD scholarship granted by CNRS.

#### **Author contributions**

C.M, B.L. and B.F. performed magnetization measurement. A.C., U.G. and D.M. designed and fabricated the array of Hall sensors. L.D, X.L. Z.Z. grew  $\text{Co}_3\text{Sn}_2\text{S}_2$  samples. C.M. and K.B. wrote the manuscript with comment from all authors. The study was performed under the supervision of K.B. and B.F.

## Competing interests

The authors declare no competing interests.

#### Additional information

**Supplementary information** The online version contains supplementary material available at https://doi.org/10.1038/s41535-025-00739-6.

**Correspondence** and requests for materials should be addressed to Charles Menil.

**Reprints and permissions information** is available at http://www.nature.com/reprints

**Publisher's note** Springer Nature remains neutral with regard to jurisdictional claims in published maps and institutional affiliations.

Open Access This article is licensed under a Creative Commons Attribution-NonCommercial-NoDerivatives 4.0 International License, which permits any non-commercial use, sharing, distribution and reproduction in any medium or format, as long as you give appropriate credit to the original author(s) and the source, provide a link to the Creative Commons licence, and indicate if you modified the licensed material. You do not have permission under this licence to share adapted material derived from this article or parts of it. The images or other third party material in this article are included in the article's Creative Commons licence, unless indicated otherwise in a credit line to the material. If material is not included in the article's Creative Commons licence and your intended use is not permitted by statutory regulation or exceeds the permitted use, you will need to obtain permission directly from the copyright holder. To view a copy of this licence, visit http://creativecommons.org/licenses/by-nc-nd/4.0/.

© The Author(s) 2025